

2017

Design and Development of a Flapping Wing System for Unsteady Forces and Power Measurement

Durlav Mudbhari
Lehigh University

Follow this and additional works at: <http://preserve.lehigh.edu/etd>



Part of the [Mechanical Engineering Commons](#)

Recommended Citation

Mudbhari, Durlav, "Design and Development of a Flapping Wing System for Unsteady Forces and Power Measurement" (2017).
Theses and Dissertations. 2736.
<http://preserve.lehigh.edu/etd/2736>

This Thesis is brought to you for free and open access by Lehigh Preserve. It has been accepted for inclusion in Theses and Dissertations by an authorized administrator of Lehigh Preserve. For more information, please contact preserve@lehigh.edu.

Design and Development of a Flapping Wing System for Unsteady Forces and Power Measurement

by

Durlav Mudbhari

A Thesis

Presented to the Graduate and Research Committee

of Lehigh University

in Candidacy for the Degree of

Master of Science

in

Mechanical Engineering and Mechanics

Lehigh University

December 2016

© Copyright 2016 by Durlav Mudbhari
All Rights Reserved

Certificate of Approval

This thesis is accepted and approved in partial fulfillment of the requirements for the Master of Science in Mechanical Engineering and Mechanics.

Date

Keith Moored
(Thesis Advisor)

Gary Harlow
(Chairperson of Department)

Acknowledgements

There have been far too many people to mention individually who have assisted me in so many ways during my Lehigh career. Without their support and assistance, the completion of this thesis would not have been possible.

I have my deepest appreciation to my beloved mom, dad and my sisters for their inexhaustible tolerance and support. I am grateful to my friends in Nepal as well as in the US who always believed in me and pushed me beyond my limits to pursue my goals.

I am enormously grateful to my advisor, Professor Keith Moored, for his valuable guidance, inspiration and support. It is his supervision and help that led me down intellectual paths I would not otherwise have traversed. I am thankful to Eli Towne, Dick Towne, Bill Maroun and Ed Force for all their assistance and guidance in construction of all wind tunnel testing equipment. I would also like to thank my fellow undergraduate researchers Kai He, Daniel Bateman, and Malcolm Erdogan for assisting me through the various phases of this project. Last but not the least, I would like to extend my sincerest appreciation to all the staff of the Mechanical Engineering Department for their support and care throughout my undergraduate and graduate years at Lehigh University.

Table of Contents

Certificate of Approval	iii
Acknowledgements	iv
List of Figures	vii
Abstract	1
1 Introduction	2
2 System Design	6
2.1 Hardware Design	7
2.1.1 Force Measurement System	9
2.1.2 First Generation Design	10
2.1.3 Second Generation Design	11
2.2 Vacuum Chamber Setup	12
2.3 Software Design	13
2.3.1 Control Center	14
2.3.2 Servo Control	15
2.3.3 Servo Input/Output Position Processing	16
3 Experiment Design	18
3.1 Wing Design	18
3.2 Experimental Procedure	19
4 Results And Discussion	21
4.1 Power Measurements	22
4.2 Force Measurements	26
4.2.1 Digital Filtering of Force Sensor Data	29
4.3 Number of Flapping Cycles Required for C_T Convergence	31
5 Conclusions	33
5.1 Future Work	35
Bibliography	36

A Amplitude Calibration	40
Vita	42

List of Figures

2.1	Experimental Setup	6
2.2	Actuation Setup	8
2.3	Air Bearing Platform for Lift/Thrust Measurement	10
2.4	First Generation Aluminum Actuation Setup	11
2.5	Vacuum Chamber Setup	13
2.6	MATLAB Control Center	14
3.1	Schematic of a Functionally-graded Flexible Wing	18
3.2	Test Wing	19
4.1	Scatter Plot of Coefficient of Power with Standard Error vs Reduced Frequency for 100% Rigid Wing in Wind Tunnel and Vacuum Chamber	23
4.2	Scatter Plot of Coefficient of Power with Standard Error vs Reduced Frequency for 33% Rigid Black Wing in Wind Tunnel and Vacuum Chamber.	23
4.3	Scatter Plot of Coefficient of Power with Standard Error vs Reduced Frequency for 50% Rigid Blue Wing in Wind Tunnel and Vacuum Chamber.	24
4.4	Coefficient of Power (with Standard Errors) vs Reduced Frequency for 100% Rigid Wing in Wind Tunnel, Vacuum Chamber, and the Net Results.	25
4.5	Coefficient of Power (with Standard Errors) vs Reduced Frequency for 33% Rigid Black Wing in Wind Tunnel and Vacuum Chamber, and the Net Results.	25
4.6	Coefficient of Power (with Standard Errors) vs Reduced Frequency for 50% Rigid Blue Wing in Wind Tunnel and Vacuum Chamber, and the Net Results.	26
4.7	Coefficient of Thrust (with Standard Errors) vs Reduced Frequency for 100% Rigid Wing	27
4.8	Coefficient of Thrust (with Standard Errors) vs Reduced Frequency for 33% Rigid Black Wing.	27
4.9	Coefficient of Thrust (with Standard Errors) vs Reduced Frequency for 50% Rigid Blue Wing.	28
4.10	FFT of Unfiltered Force Reading at 2.5Hz Flapping Frequency.	30
4.11	FFT of Filtered Force Reading at 2.5Hz Flapping Frequency.	30
4.12	FFT of Unfiltered Torque Reading at 2.5Hz Flapping Frequency.	31

4.13 Test for Number of Flapping Cycles Required for C_T Convergence. . .	32
A.1 Post Amplitude Calibration Servo Position Output vs Time	41

Abstract

Flyers and swimmers flap their wings and fins to propel themselves efficiently over long distances, maneuver in tight spaces and navigate silently to avoid detection by prey. A key element to achieve these amazing feats is the flexibility of their propulsors. While numerous studies have shown that homogeneously flexible wings can enhance force production and efficiency, animals actually have wings with varying flexural rigidity along their chord and span. The goal of this study is to design and develop an experimental setup that would help understand and characterize the force production and energetics of functionally-graded, chordwise flexible wings. A flapping wing composed of a rigid and a flexible region, that define a chordwise gradient in flexural rigidity, is used to model functionally-graded materials. By varying the ratio of the lengths of the rigid to flexible regions, the flexural rigidity of the flexible region, and the flapping frequency, the thrust production of a functionally-graded wing is directly measured. An unsteady force and torque measurement system is developed to measure the lift/drag forces and power consumption during flapping wing flight in wind tunnel. A novel vacuum chamber apparatus is developed to be used in conjunction with the wind tunnel measurements to reliably measure the aerodynamic power input and the propulsive efficiency.

Chapter 1

Introduction

Bird flights and the associated aerodynamics have always been a chief source of inspiration for aviation enthusiasts and researchers. Birds can fly in a variety of fascinating modes such as high speed, high maneuverability, long endurance, and low noise to near-silent flights. While early engineers and researchers were inspired by the ability of birds to soar in the sky, today's scientists are looking for answers that aim to solve issues ranging from broad to very specific engineering challenges. One significant element of a bird's flight is the presence of flexible wings and its associated aerodynamic impacts. Birds have evolved to develop flexible wings even though they could have evolved to fly with rigid wings. This natural evolution of birds to possess flexible pair of wings has led several studies aimed in understanding the underlying scientific reason.

Studies have shown that flexible wings can enhance force production and propulsive efficiency as well as reduce the noise of a fixed or flapping wing (Heathcote et al., 2008; Miao and Ho, 2006; Sarradj et al., 2011). Both empirical (Bozkurttas et al., 2006; Toomey and Eldredge, 2008; Heathcote et al., 2008) modelling (Mittal et al., 2006; Alben, 2008; Michelin and Smith, 2009) and computational studies (Vanella et al., 2009; Young et al., 2009; Le et al., 2010; Kang et al., 2011) have indicated that

flexible propulsors can enhance thrust production. In several studies, wing flexibility has also been evaluated in material properties of the propulsor such as elastic modulus (Heathcote et al., 2008; Kang et al., 2011) or flexural rigidity (Tangorra et al., 2010; Combes and Daniel, 2001, 2003).

In animals and flyers, bending has been projected to occur both evenly over the span (Kang et al., 2011; Miao and Ho, 2006) as well as over a limited portion (Villanueva et al., 2011; Colin et al., 2012) of the propulsor. One study has shown that over a wide spectrum of swimmers and flyers, rather than an even span-wise bending of the propulsor, only a fixed portion of the propulsor actually bend (Lucas et al., 2014), suggesting that wing bending in animals and flyers is not fully homogeneous. While a lot these studies have shown that homogeneously flexible wings can enhance thrust production and propulsive efficiencies, animals actually have wings with varying flexural rigidity along their chord and span. Similarly, while some bending can be beneficial, excessive bending can actually diminish thrust production efficiency (Liu and Bose, 1997; Heathcote et al., 2008). However, much research has yet to be done to completely understand the role of non-homogeneous wing flexibility on its performance.

Understanding the role of wing flexibility will have broader impacts on sustainability and the environment and will also be very crucial in developing the next generation of swimming and flying marvels. One outcome of this work will be to enhance the development and design of the next generation of small, efficient and maneuverable Autonomous Underwater Vehicles (AUV). Such devices could be used to effectively monitor terrestrial and aquatic animal populations (Fish et al., 2003) or to monitor pollutants in waterways, bays and oceans (Listak et al., 2005). Use of flexible wings in such AUVs would be greatly beneficial as it could complement or even substitute traditional powering methods such as propellers. Using flexible wings to enhance lift and thrust production (Ramanarivo et al., 2011) would increase the propulsive ef-

efficiency (Dai et al., 2012) while reducing costs and limitations associated with using generic powering techniques. This could in effect reduce the size of AUVs, letting engineers feasibly develop smaller AUVs that are more maneuverable and can reach to geographically inaccessible underwater locations.

Another outcome would be the development of efficient wave energy extraction devices based on flapping wing technology that will reduce the fuel consumption of large-scale shipping vessels; a major source of global pollution (Endresen et al., 2003). Studies have shown that the use of flexible wings as stabilizers in naval vessels result in improved propulsive efficiency; reducing their fuel consumption and greenhouse gas emissions. Ship stabilizers are airfoil like structures called hydrofoils that are designed and employed in naval vessels to dampen or dissipate the kinetic energy generated by the sea waves. However, these hydrofoils do more than just dampening the unwanted vessel motion generated by the sea waves. A 174 ton Russian vessel that used a passive hydrofoil stabilizer was able to increase the engine power by 45 – 87%, while also simultaneously reducing the ship motion by a factor of 2 – 2.5 (Nikolaev et al., 1995). Similarly in another experiment, a hydrofoil mounted to elastic links on a 180ton research vessel cruising at 15*knots* supplied 22% of the thrust in conjunction with the conventional propeller. The hydrofoil was also able to propel the ship at 8*knot* speeds when the propeller was turned off by extracting energy from the sea waves. The key to enhancing thrust production as well as dampening unwanted motion in naval vessels could well possibly be the proper design of flexible hydrofoils. Implementation of well-designed flexible hydrofoils could improve propulsive efficiency in the vessels, which in return would lower the fuel consumption as well as the economic cost and environmental impact of surface vessel transportation.

With an end goal of understanding the role of flexible wings in swimmers and flyers, the objective of this project was to design and develop functionally-graded flexible wings as well as a system capable of generating flapping wing motion, mim-

icking a bird's flapping wing flight, to understand the physics of flexible wings by measuring the associated unsteady forces and power. Using the system, the data collected through flapping wing experiments of flexible wings could help shed light on the effects of and the relationship between flexible wings and the various aerodynamic performance parameters of interest such as lift, thrust, and propulsive efficiency. To study the effects of flexibility, functionally-graded flexible wings, explained in detail in section 3.1, are fabricated with aspect ratio of 2, corresponding to that of forest-dwelling birds (Johnson, 1997). Flexibility will be varied systematically in the chord-wise direction, the span-wise direction, and in both directions simultaneously. By changing the material properties as well as the ratio of wing rigidity to flexibility, the effects of wing flexibility on its performance will be studied. Each configuration of the wing will undergo some crucial dynamic motion testing, by flapping at a range of frequencies. Force transducers will measure three major components of the wing performance: lift, thrust, and power input. Flow visualization techniques can also be used to connect the forces and performance with the flapping wing vortex dynamics. The quantitative and qualitative results would help in understanding the underlying physics of biological flight.

Chapter 2

System Design

Using previous unsteady force and power measurement studies (Dewey et al., 2013) as a source of design inspiration, an actuation mechanism was developed. The actuation mechanism is connected to a computer using Data Acquisition (DAQ) instruments and controllers. The actuation mechanism is the physical mechanism responsible in generating flapping wing motion as well as recording force and torque measurements. An image of the wind tunnel experimental setup is shown in Figure 2.1.



Figure 2.1: Experimental Setup

2.1 Hardware Design

The wind tunnel is an Eiffel tunnel designed by Engineering Laboratory Design Inc. The test section of the wind tunnel measures 32" X 18" X 18", and consists of transparent acrylic plates on all four sides. The top plate of the test section is removable for access to the test section. However, the top section is modified to have two 6" diameter removable acrylic windows. One of the windows also has a 4.5" X 0.5" slot through which the test wing shaft passes to the actuation setup. It is also this slot in which the wing shaft oscillates. The other circular window is mainly used as an access port when attaching or removing the wing from the actuation setup. A United Sensor PCD-5-KL pitot tube is permanently fixed off the center upstream of the test section. The pitot tube ports are connected to a Dwyer MS2 pressure sensor that can read dynamic and static pressure difference of up to 25Pa. The pressure sensor is connected to the DAQ card to calculate air speed directly using Bernoulli's equation.

$$\frac{v^2}{2} + gz + \frac{P}{\rho} = constant \quad (2.1)$$

where v is the air speed, P is the pressure, and ρ is the air density.

The actuation mechanism consists of the actuation setup connected to the force sensor. In the actuation setup, a servo is suspended horizontally on a torque sensor. This allows the torque on the servo to be read by the torque sensor. The torque sensor used is an Omega TQ202-50 and is rated at 5.6Nm. An ultra high speed standard servo, RFX FS-0521HV, is used in the actuation system. The servo offers 2.1Nm of torque and 0.05s transit speed. The servo head is connected to a S1-5000 US Digital optical encoder using a 0.25" aluminum drive shaft. The optical encoder reads instantaneous position of the shaft. This drive shaft is suspended from two columns, and held in place by bearings attached to the columns. Furthermore, the portion of this drive shaft between the two bearings consist of a shaft coupler to which

the shaft of the test wing is attached. Thus, when the servo rotates, this drive shaft rotates, allowing the wing to produce a flapping motion. The torque sensor and the optical encoder are housed in a small frame that is fabricated using Fused Deposition Modeling (FDM) process. This frame along with these sensors and servo, is what is referred to as the actuation setup. A picture of the actuation setup showing the electrical components is shown below in Figure 2.2.

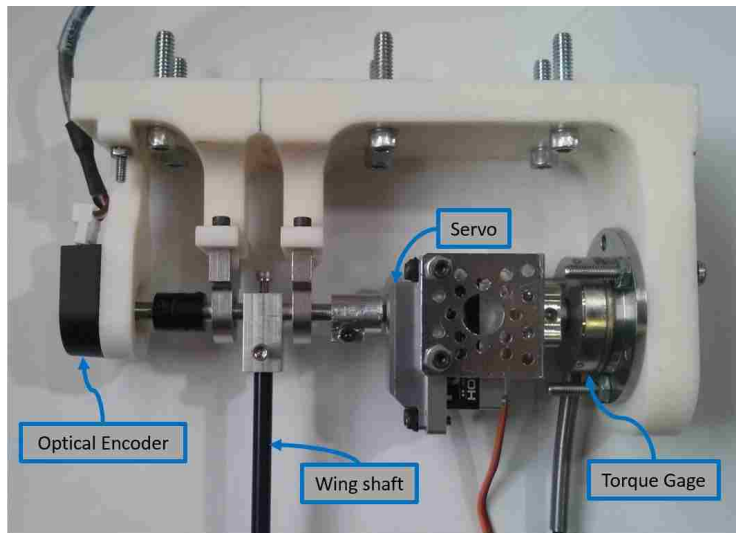


Figure 2.2: Actuation Setup

The actuation setup is attached to an acrylic plate forming a platform that is suspended on three New Way air bearings. Compressed gas is passed on to these air bearings at 60psi to freely suspend the load of the platform. Initially, the compressed gas used was dry Nitrogen supplied by PraxAir compressed gas cylinder. However, over the course of a year, restocking the gas cylinder periodically turned out to be economically and logistically inconvenient. Therefore, an air compressor was used to replace the Nitrogen gas system. Since the air bearings need dry air to prevent rusting of the exposed metal parts, an air compressor with air drying and filtration unit is used. A California Air Tools, 10010DCAD, air compressor was purchased and connected to the air bearing system. The compressor compresses air and stores it in the 10Gallon storage tank at about 120psi and supplies it at about 60psi through the

outlet. Once the internal tank pressure is too low to supply outlet pressure of 60psi , the compressor kicks in and starts compressing gas again and storing it in the tank.

Initially single point load cells were used for force measurements. Omega LCAE-600, LCAE-3000, and Phidgets CZL639HD force sensor rated at $100g$ were used in the system. However, all of these three sensors couldn't resolve the small forces generated during test cycles, without compromising the measurement range. Therefore, a six axis ATI Nano-43 sensor was implemented in the system which has a $0.001953N$ resolution and $9N$ range. Even though the ATI sensor has six axis measurement capability offering both force and torque measurements, only single Z-axis measurements were read to obtain thrust/drag measurements. This was done in order to avoid redesigning the system with the ATI sensor incorporated to measure force and torque. Torque sensor signals were amplified using an Omega DMD4059 signal conditioner. To acquire data from all the sensors, a high speed National Instruments (NI) PCIe6353 daq card was used in conjunction to a NI SCB-68A connector block. In addition, a Pololu Micro Maestro servo controller was used to communicate with the servo. This actuation and data acquisition system was all controlled in MATLAB through a in-house built control center described in a later section.

2.1.1 Force Measurement System

The experimental setup was designed to measure unsteady forces during wing flapping cycles. The use of three air bearings allowed to freely suspend the actuation platform to measure forces without any frictional effects. The design of the air bearing suspension system gave two possible configuration, allowing the measurement of both the thrust and lift forces, albeit, only one force could be measured during any given experiment. Since lift and thrust act in perpendicular direction, the air bearing suspension platform could be rotated 90° to switch from one force measurement configuration to another. An image of the air bearing platform in thrust configuration is

shown in Figure 2.3

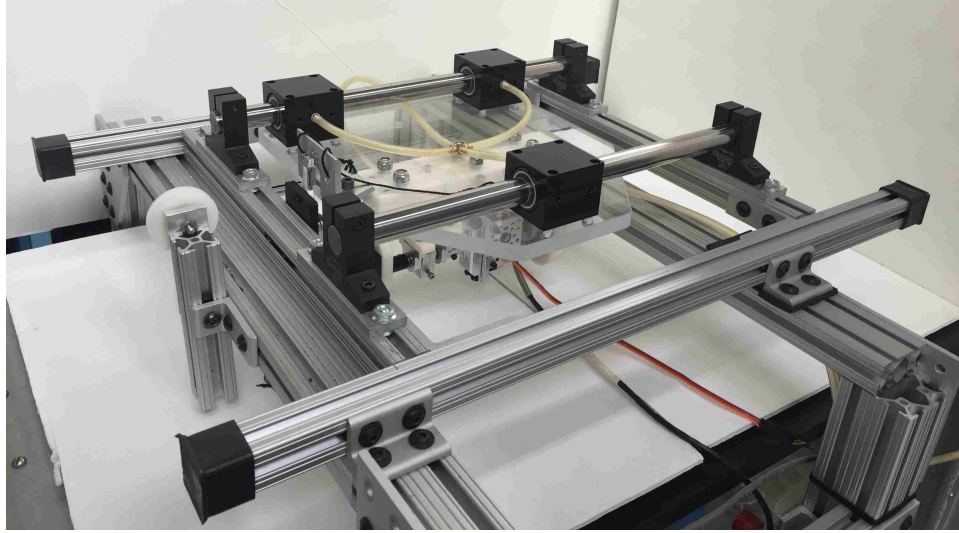


Figure 2.3: Air Bearing Platform for Lift/Thrust Measurement

When the system was configured to measure thrust and drag forces, a mass of 500g was suspended from the platform, providing an offset force in the thrust direction. This offset weight was placed to ensure that the platform was in full contact with the force gage at all times, even when it generated drag, without requiring any actual physical connection such as screws and nuts. This resulted in all thrust and drag forces measured to be oscillating about the 500g load offset which was later negated from the sensor readings during the data acquisition process. This negation ensured that the force readings obtained were true readings without any bias.

2.1.2 First Generation Design

While the design of the overall system didn't change significantly from the first proof of concept, major improvements have been made to the design after running mock tests and identifying design issues. An early design of the actuation setup, shown in Figure 2.4, consisted of aluminum frame to house the sensors. This aluminum housing was hung from the acrylic platform using a 1" X1" X1" aluminum channel. The frame itself had a tall profile resulting a significant distance between the drive shaft and the acrylic

plate on which the aluminum channel was attached. This tall profile coupled with the fact that the aluminum housing was constructed by assembling several aluminum plates together caused vibrational issues that were identified by performing a Fast Fourier Transform (FFT) of force sensor data in the lift measurement configuration. To address these vibrational issues, it became necessary to lower the profile of the actuation setup, and also change the way the actuation setup was assembled.

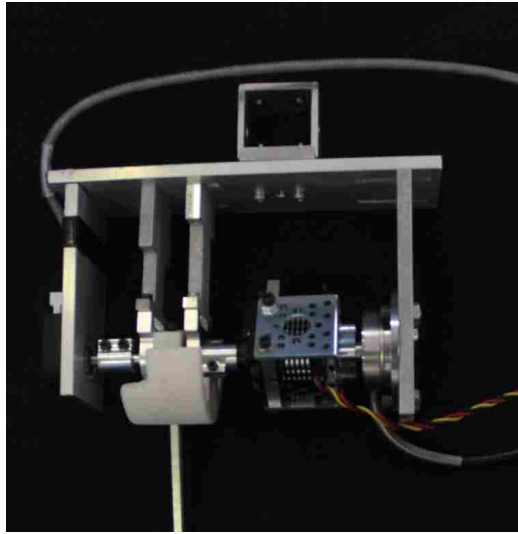


Figure 2.4: First Generation Aluminum Actuation Setup

2.1.3 Second Generation Design

Since using aluminum plates to assemble the actuation setup would result in a vibration-prone system, the actuation setup frame design was modified to be manufactured using additive manufacturing process. Using FDM technology offered by Stratasys machine, a new actuation setup housing was developed. As it can be seen in Figure 2.2, the overall profile of this new actuation setup is much lower which resulted in improvement in vibrational issues faced in the earlier aluminum housing design.

2.2 Vacuum Chamber Setup

A novel vacuum chamber system was developed to measure inertial power consumption. A Belart Techni-Dome Vacuum Dessicator that could hold items up to 45cm tall was used as the choice of vacuum chamber. The Techni-Dome dessicator consisted of two laboratory grade polycarbonate domes. Although the dessicator came with a sealing gasket taped to the lower dome, Momentive RTV 102 silicone sealant was used to ensure proper sealing of the gasket to the dome. Through the gasket, 22 gage copper pins were carefully inserted and trimmed. The copper pins would act as a conductor to transmit data and control signals in and out of the vacuum chamber. A towering structure was constructed out of 8020 aluminum extrusions that allowed holding the actuation system inside the vacuum chamber. The towering structure was constructed in a way to permit any desired motion or the same motion coverage as in the wind tunnel experiments. Rubber dampers were attached at the four legs of the towering structure, and was then placed on the bottom dome and levelled. The top dome could then be placed over the gasket and vacuum pump be used to achieve vacuum. To avoid vibration of the vacuum chamber system at high flapping frequencies, a flanged dome holder was fabricated using FDM process. This flanged dome holder would attach to the bottom surface of the lower dome and could then be clamped to the table. The vacuum pump achieved a little over 28.5 inches of Mercury gage pressure, equivalent to about 95% vacuum. An image of the vacuum chamber setup during testing is shown in Figure 2.5.

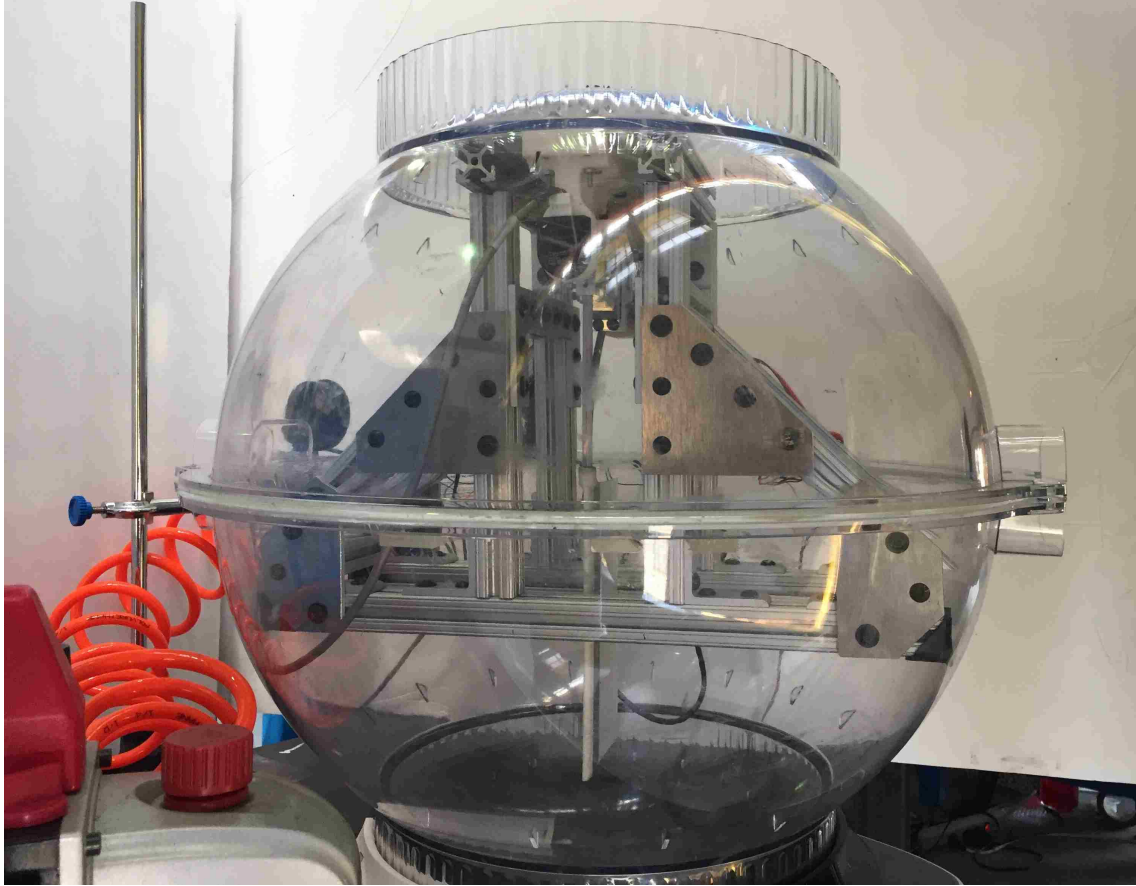


Figure 2.5: Vacuum Chamber Setup

2.3 Software Design

To measure unsteady forces, it was important to both control actuation mechanisms, as well as, read all the signals at proper timestamps. Due to this, it was crucial to develop a stand-alone control program where the user could input all experiment parameters and precisely control wing actuation and measure the loads generated. Initially, a LabVIEW Virtual Instrument (VI) program was developed to control the servo as well as to record the force, torque and position data. However, it was later determined that the control program needed to not only control sensors, but it also needed to perform various other sensor related tasks, such as taring, calibrating, and post processing signals. Therefore, a new control center was developed in MATLAB

that could calibrate, tare and control sensors, as well as process the acquired data, and analyze results without requiring any data transfer or a change in software platform.

2.3.1 Control Center

MATLAB offered a graphical user interface development environment known as Graphical User Interface Design Environment (GUIDE). MATLAB GUIDE was used to create the master Control Center where performing all the tasks needed to run an experiment, from the very beginning of instrument calibration to the end of signal processing and graphs generation after an experiment, was possible. A screenshot of the Control Center is shown in Figure 2.6.

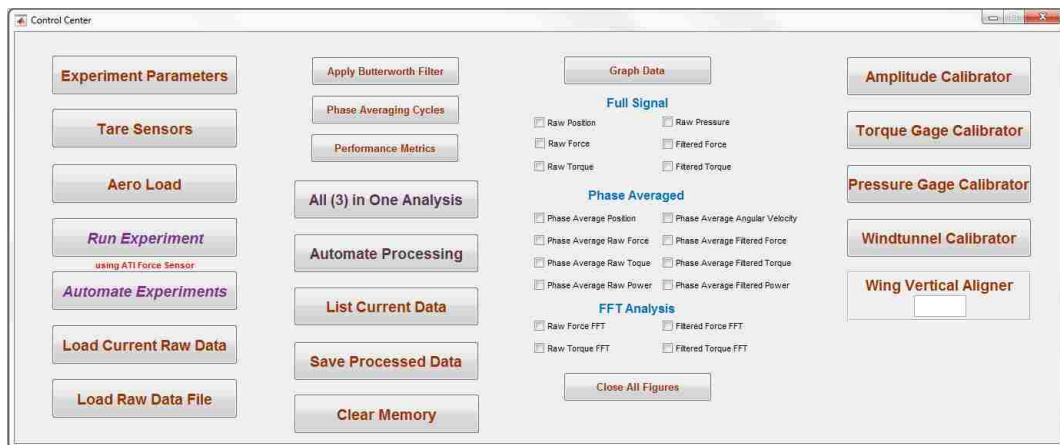


Figure 2.6: MATLAB Control Center

Since MATLAB GUIDE used callback functions as a way to invoke response, the MATLAB code for the Control Center was very modular and readable. All the parameters of interest during the course of using the Control Center were stored in the MATLAB workspace as a structure for easy access and modification. The Master Control Center was fully capable of automating flapping wing experiment through a range of flapping frequency, saving the acquired data, processing them and producing and comparing desired results for all test cases at once. In addition, it was capable of producing various graphs for raw, filtered and processed data. Lastly, the Control

Center could run diagnostics on the frequency response of the force and torque sensor readings to understand vibrational effects, and potentially filter them digitally as needed.

2.3.2 Servo Control

Since a servo was the motion generator in this designed system, it was important to understand how servo worked, and how Pololu controller could be programmed to communicate with it to generate the desired motion. The Pololu Controller communicated with the servo through binary instruction packets of Pulse-width Modulation (PWM) signal. Therefore, any desired servo position (in degrees angle) needed to be first converted to the corresponding PWM signal then to the corresponding binary data packet.

Although, not necessarily exactly true for all standard servo, the width of the 8-bit neutral point pulse for the servo used in this system was $1500\mu s$, meaning a PWM signal of $1500\mu s$ made the servo attain and hold a position of 90° . Similarly, a pulse of $992\mu s$ corresponded to 0° , while a pulse of $2000\mu s$ corresponded to 180° . Since the desired motion was a symmetric flapping motion, the 90° neutral point of the servo was designated to be the 0° amplitude of the wing flapping motion. This would mean that for the wing to be at its neutral position, a PWM signal of $1500\mu s$ would need to be passed to the servo.

The PWM signal for the servo position was transmitted to the servo by the Pololu Controller using Compact Protocol. The Maestro Compact Protocol was simply:

[Command Byte, Servo Number, Low Bit, High Bit]

For example, if channel 2 was configured as a servo and the desired target was 90° , that is $1500\mu s$, then it corresponded to $1500 \times 4 = 6000 = 01011101110000$ in binary. (Corporation, 2014) Therefore, the byte sequence using Compact Protocol would be:

in binary: 10000100, 00000010, 01110000, 00101110

in hex: 0x84, 0x02, 0x70, 0x2E

in decimal: 132, 2, 112, 46

A snippet of MATLAB code to control the servo is shown below.

```
function funcServoControl(servoNumber,servoAngle)
% servoNumber = channel # on pololu on which servo to be
% controlled is attached
% servoAngle = desired/destination servo angle in degrees
% Degrees of angle converted to microseconds of PWM signal
pozInTimeServo = round((servoAngle*10+1500)*4);
% PWM signal broken down to low bit and
% high bit for instruction packet
lowPozTargetServo = bitand(pozInTimeServo,127);
highPozTargetServo = bitshift(bitand(...
pozInTimeServo,16256),-7);
% Serial object is created here for servo communication
pololuServo = serial('COM5',...
'Baudrate',38400,'DataBits',8,'Parity','none');
% Serial port is opened for the object
fopen(pololuServo);
% instruction packet written on the serial port
fwrite(pololuServo,...
[132,servoNumber,lowPozTargetServo,highPozTargetServo],
...
'uint8');
% close the port after the servo moves to desired angle
fclose(pololuServo);
% delete the port to clean memory
delete(pololuServo);
```

2.3.3 Servo Input/Output Position Processing

Like most mechanical devices, a servo has its physical limitations too. Assuming the load on a servo is well within its capacity and that it is given enough time to move, the servo will reach its desired angle target. However, as the time between two consecutive target position instructions is decreased and the amplitude of motion is increased, the limitations of servo kick in. When the servo is prescribed a harmonic

motion of varying frequency and amplitude, the reaction time between one position to another position decreases and the servo is unable to reach the desired position target at any given instant, hence undershooting. This undershooting motion is evident during the experiment when the servo is prescribed a harmonic motion of low flapping frequency. On the contrary, for any harmonic motion, if the load on the servo is large enough, then the inertia can actually cause the servo to overshoot. This overshooting motion is evident during the experiment when the servo is loaded with heavier wings and is prescribed a harmonic motion of high flapping frequency. Because of the undershooting and overshooting nature of the servo at various experimental conditions, it was important to amplify or deamplify the prescribed amplitude to reach the desired amplitude of motion. The method of amplifying or deamplifying the input amplitude to get correct output amplitude is detailed in Appendix A.

Chapter 3

Experiment Design

3.1 Wing Design

While a lot of studies have shown that homogeneously flexible wings can enhance thrust production and propulsive efficiencies, animals actually have wings with varying flexural rigidity along their chord and span. Therefore, to understand the role of wing bending as well as the role of flexural rigidity in flight aerodynamics, a functionally-graded wing was designed. A functionally-graded chordwise flexible flapping wing composed of a rigid and a flexible region, that define a chordwise gradient in flexural rigidity, was used to model functionally-graded materials.

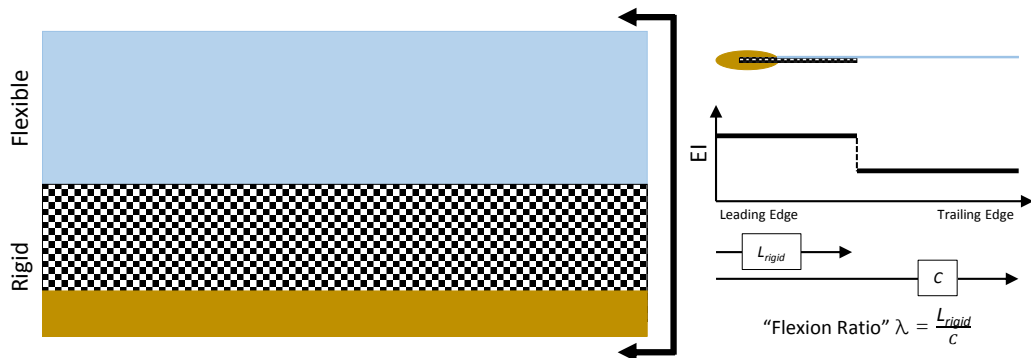


Figure 3.1: Schematic of a Functionally-graded Flexible Wing

Wings of 19.05cm span (b), 9.53cm chord (C), rectangular cross-section and plan-form are constructed for the experiment. The aspect ratio, $AR = 2$, was held constant for all the wings. The ratio of the lengths of the rigid section to chord length, defined as flexion ratio (λ), and the flexural rigidity (D) of the flexible region was varied to obtain wing of varying flexibility. The wings were composed of carbon fiber panels of constant thickness, 0.79375mm , and plastic shim of varying thickness manufactured by Artus Corp. The variation of plastic sheet thickness, indicated by different colors, was to obtain a wide range of flexibility in the flexible region of the wing. Increasing plastic shim thickness decreased its flexibility. The leading edge of the panel was attached to a fairing manufactured using FDM process. This leading edge fairing was a partially-open rounded sheath designed to suppress leading edge separation observed in flat plates, and extended from the base to the wing tip. The base of this leading edge coupler also had a design feature that allowed attachment to the carbon fiber wing shaft, which was then attached to the coupler in the actuation system.

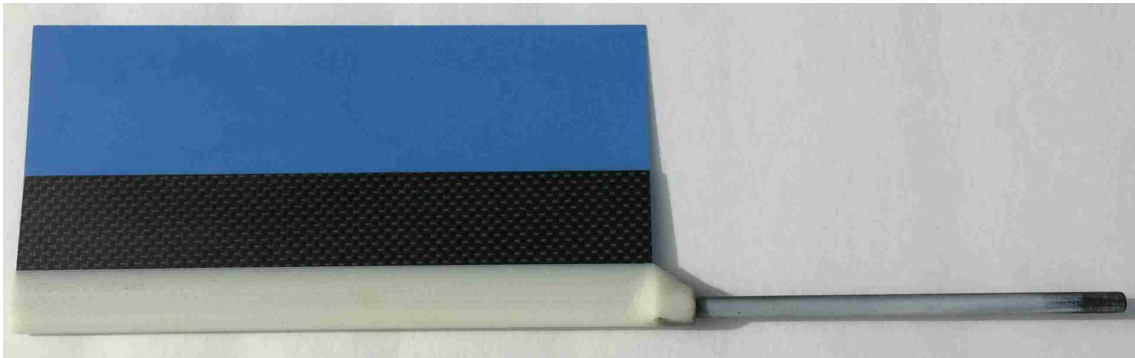


Figure 3.2: Test Wing

3.2 Experimental Procedure

Once the system design and wing design was complete, and the hardware and software were integrated, tests were run to examine if the system was running up to the requirements. To check the performance and robustness of the system, experiments

were conducted in both wind tunnel and vacuum chamber for each wing type. Each set of experiment consisted of three trials of frequency sweep from 0 to $4.75Hz$ at $0.25Hz$ increments. Wind tunnel and vacuum chamber tests were alternated after every set. To do so, the actuation system would be disconnected from the wind tunnel air bearing platform and connected to the vacuum chamber towering structure after the first set of wind tunnel test was completed. Then, at the end of one set of vacuum chamber test, the actuation system would again be moved back to the wind tunnel. Since moving the actuation system back and forth between wind tunnel and vacuum chamber could potentially give rise to more sources of errors due to experimental inconsistencies such as platform leveling and wing pitch alignment, this method was adopted to check the robustness and reliability of the system to produce repeatable results.

The servo in the actuation system was numerically controlled using MATLAB to generate sinusoidal motion of some input amplitude and frequency. Because of the physical limitations of the servo, the upper limit of sinusoidal flapping motion that could be generated was at about 40° peak-to-peak amplitude at $4.75Hz$ flapping frequency. Therefore, a frequency (f) range of 0 to $4.75Hz$ at $0.25Hz$ increments was chosen with a fixed peak-to-peak amplitude (A) of 40° . Altogether, 20 evenly spaced frequencies, corresponding to reduced frequencies from $k = \pi fC/U_\infty$, were examined for each wing. For majority of the test cases, the peak-to-peak amplitude and flapping frequency varied by less than 3% and 1% respectively from the input values. The pitch angle was held constant at 0° , and 30 flapping cycles were generated for all test cases. Wind tunnel experiments were performed at a wind speed (U_∞) of $3ms^{-1}$. Therefore, Reynolds number (Re) of the order of 15000 and Strouhal Number ($St = fA/U_\infty$) range of $0 < St < 0.3$ was achieved. Note that the Strouhal Number is calculated based on input peak-to-peak amplitude and does not take into account the potential wing deflections during flapping cycles.

Chapter 4

Results And Discussion

For system validation tests, three sets, totalling nine trials, of measurements were obtained for the test wings in both wind tunnel and vacuum chamber. The three wings used for the validation tests were:

1. 100% Rigid Wing (referred to as Fully Rigid Wing)
2. 33% Rigid Wing with Black(0.31mm) shim (referred to as Black Wing)
3. 50% Rigid Wing with Blue(0.125mm) shim (referred to as Blue Wing)

For each test case, the time-averaged net thrust (T) and the time-averaged power input to the fluid (P) was calculated by averaging over a complete number of cycles. While the net thrust force was calculated directly from the force sensor data, the calculation of net power input to the fluid was a multi-step process. First, the average power input to actuate the wing in flight (P_a) was found by measuring the reaction torque (τ) on the servo, and the angular velocity ($\dot{\theta}$) from wind tunnel data using $P = T_p^{-1} \int_0^{T_p} \tau \dot{\theta} dt$. Then, using the same method, the average power input to actuate the inertial wing mass and overcome friction (P_f) was measured from the vacuum chamber data. The net power delivered to fluid is then $P = P_a - P_f$.

The average net thrust and average power input to the fluid are given in non-dimensional form by the coefficients of thrust, C_T , and power, C_P , where

$$C_T = \frac{T}{\frac{1}{2}\rho_f U_\infty^2 SC} \quad \text{and} \quad C_P = \frac{P}{\frac{1}{2}\rho_f U_\infty^3 SC} \quad (4.1)$$

4.1 Power Measurements

Power measurements were performed for all three sets of wings in both wind tunnel and vacuum chamber. The results were computed using the aforementioned methods. The following graphs, Figure 4.1, 4.2 and 4.3, show the coefficient of power, C_P , for the wings as a function of reduced frequency, k . As it can be seen, for all three wing cases, C_P was found to be increasing as the reduced frequency was increased. It is important to note that while in the fully rigid wing case, a monotonic increase in C_P is observed, in the case of the two flexible wings, the coefficient of power first increases until a maximum is reached, and then decreases and increases again.

In the following graphs, the coefficient of power for all nine test cases for each wing are shown in a scatter plot. On top of the scatter plot, are the two means of the coefficient of power measured in the wind tunnel and the vacuum chamber. As it can be observed, the results for various trials are repeatable and lie close to one another. It is important to note that after every set of three trials, indicated by one distinct color on the graph, the actuation setup is moved from wind tunnel to vacuum chamber, or vice versa, to run another set of three trials. In doing so, the wing is first taken out of the actuation setup, then, once the actuation setup is placed in the vacuum chamber, the wing is re-attached. The actuation setup is levelled and the tests are then continued. The errors introduced due to this movement of the actuation setup could be the sources of scatter in the coefficient of power data.

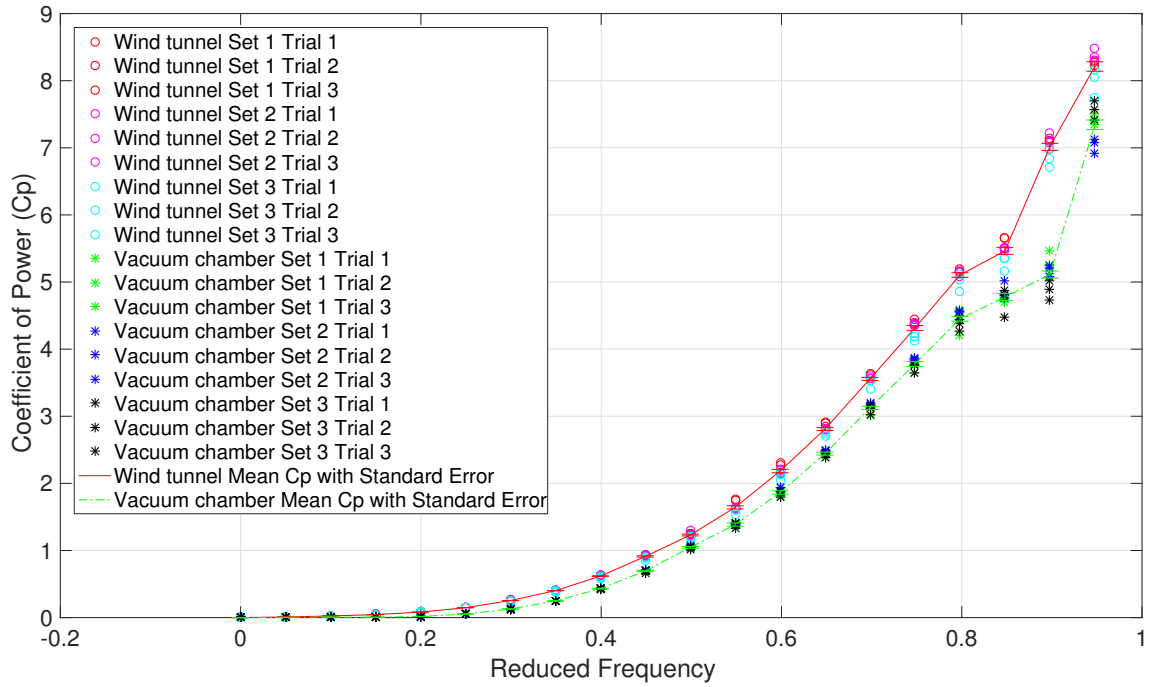


Figure 4.1: Scatter Plot of Coefficient of Power with Standard Error vs Reduced Frequency for 100% Rigid Wing in Wind Tunnel and Vacuum Chamber

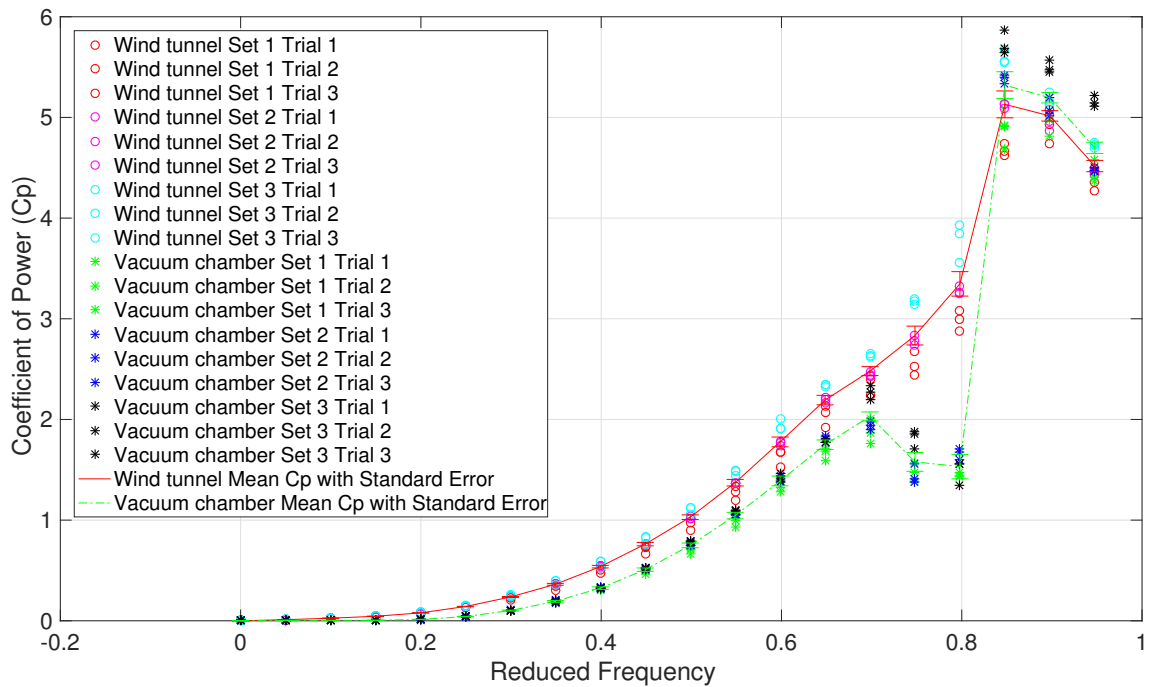


Figure 4.2: Scatter Plot of Coefficient of Power with Standard Error vs Reduced Frequency for 33% Rigid Black Wing in Wind Tunnel and Vacuum Chamber.

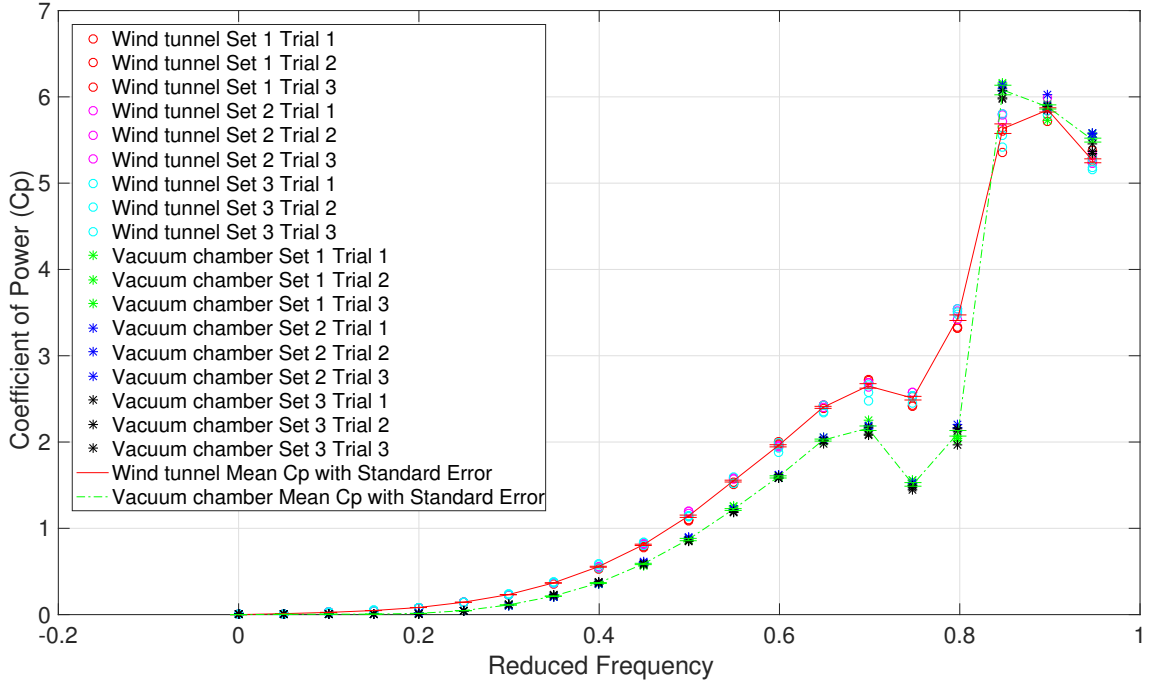


Figure 4.3: Scatter Plot of Coefficient of Power with Standard Error vs Reduced Frequency for 50% Rigid Blue Wing in Wind Tunnel and Vacuum Chamber.

It is observed that the coefficient of power for both flexible wing cases is less than that of the rigid wing. This could be a result of deflection of the plastic shim during the flapping cycles to achieve a more aerodynamically efficient shape. As described by Ramananarivo et al. (2011), the trailing edge of an oscillating flexible panel deforms with respect to the free-stream velocity to lessen parasitic flow separation at the trailing edge, thereby decreasing the torque (and power) required to sustain motion.

The novel vacuum chamber system was developed to achieve measurements of power to actuate the flapping system and overcome friction. This measurement could then be subtracted from the wind tunnel measurement to achieve pure aerodynamic power consumption during the oscillation cycles. The coefficient of power for tests inside the wind tunnel, inside the vacuum chamber, and the net of both tests are plotted on the following graphs, Figure 4.4, 4.5 and 4.6. As it can be observed, the power measurements in the wind tunnel and vacuum chamber lead to the computation of pure aerodynamic coefficient of power with very small error.

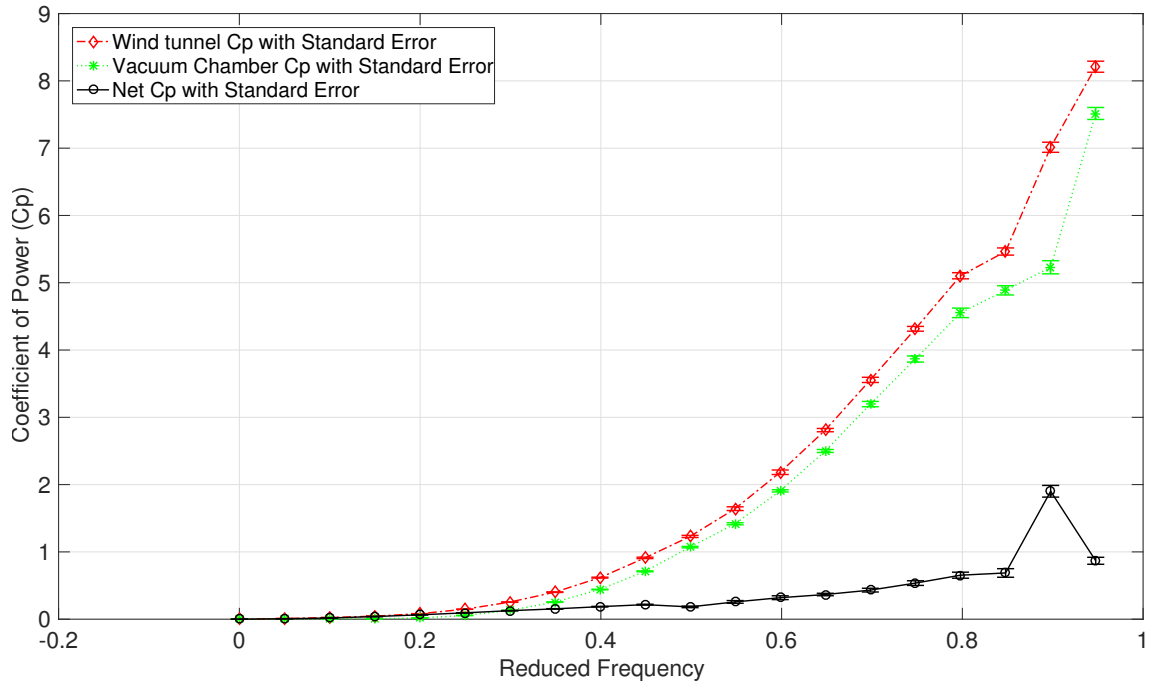


Figure 4.4: Coefficient of Power (with Standard Errors) vs Reduced Frequency for 100% Rigid Wing in Wind Tunnel, Vacuum Chamber, and the Net Results.

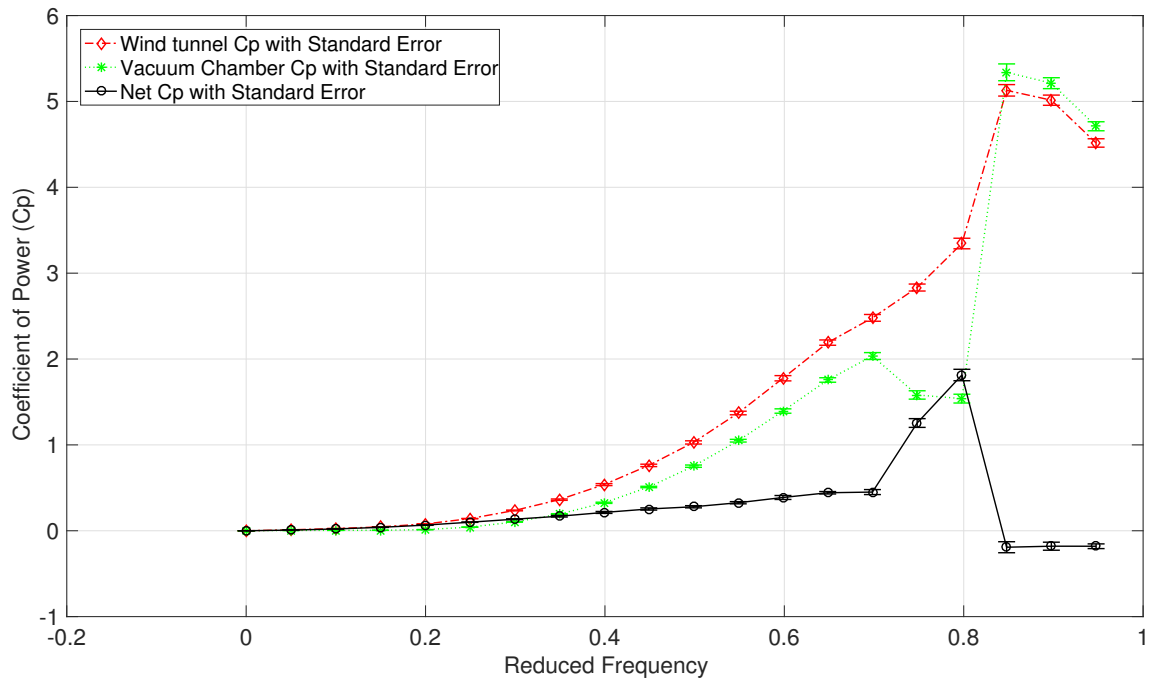


Figure 4.5: Coefficient of Power (with Standard Errors) vs Reduced Frequency for 33% Rigid Black Wing in Wind Tunnel and Vacuum Chamber, and the Net Results.

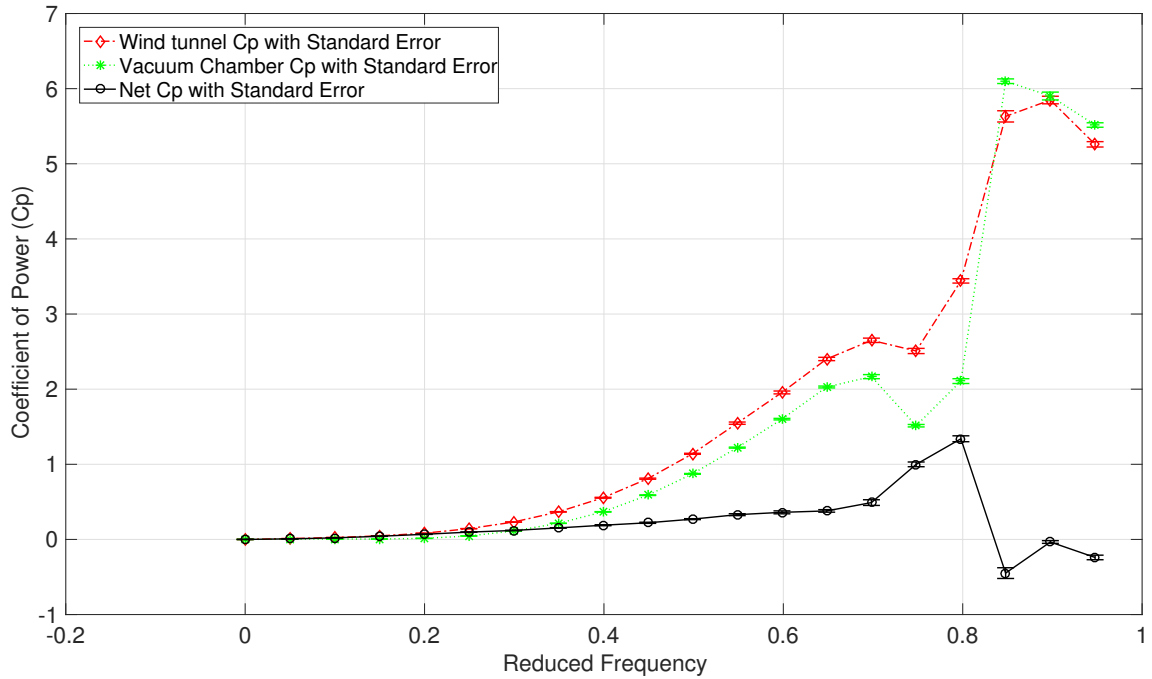


Figure 4.6: Coefficient of Power (with Standard Errors) vs Reduced Frequency for 50% Rigid Blue Wing in Wind Tunnel and Vacuum Chamber, and the Net Results.

4.2 Force Measurements

Instantaneous force measurement was carried out in the wind tunnel to compute coefficient of thrust. The actuation system suspended on free floating air bearing system was designed to allow measurement of pure thrust and drag forces. Although the ATI sensor used for force measurement was capable of measuring six degrees of force, only the measurement from the thrust/drag direction was used. The coefficient of thrust for the three wings are plotted on the following graphs, Figure 4.7, 4.8 and 4.9 .

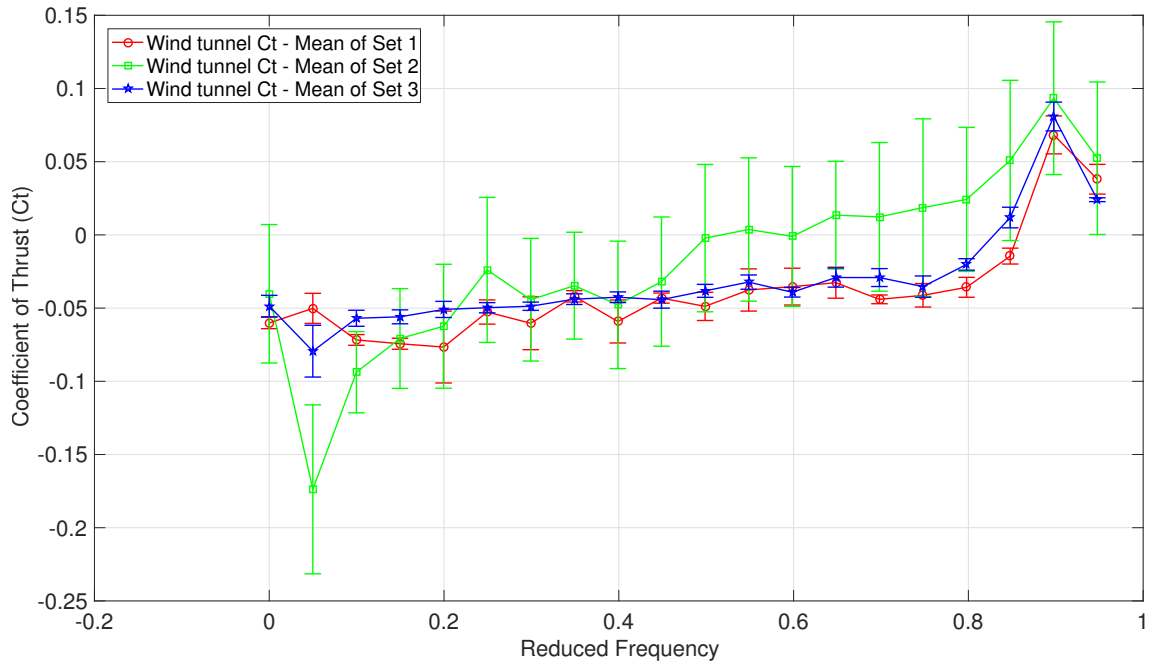


Figure 4.7: Coefficient of Thrust (with Standard Errors) vs Reduced Frequency for 100% Rigid Wing

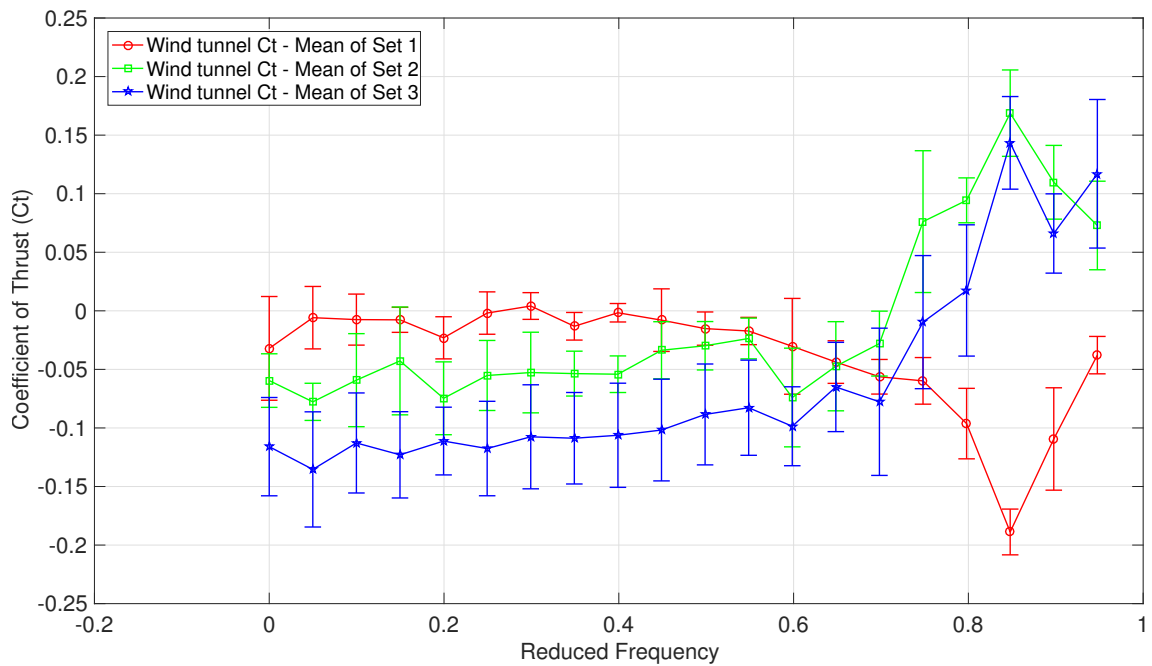


Figure 4.8: Coefficient of Thrust (with Standard Errors) vs Reduced Frequency for 33% Rigid Black Wing.

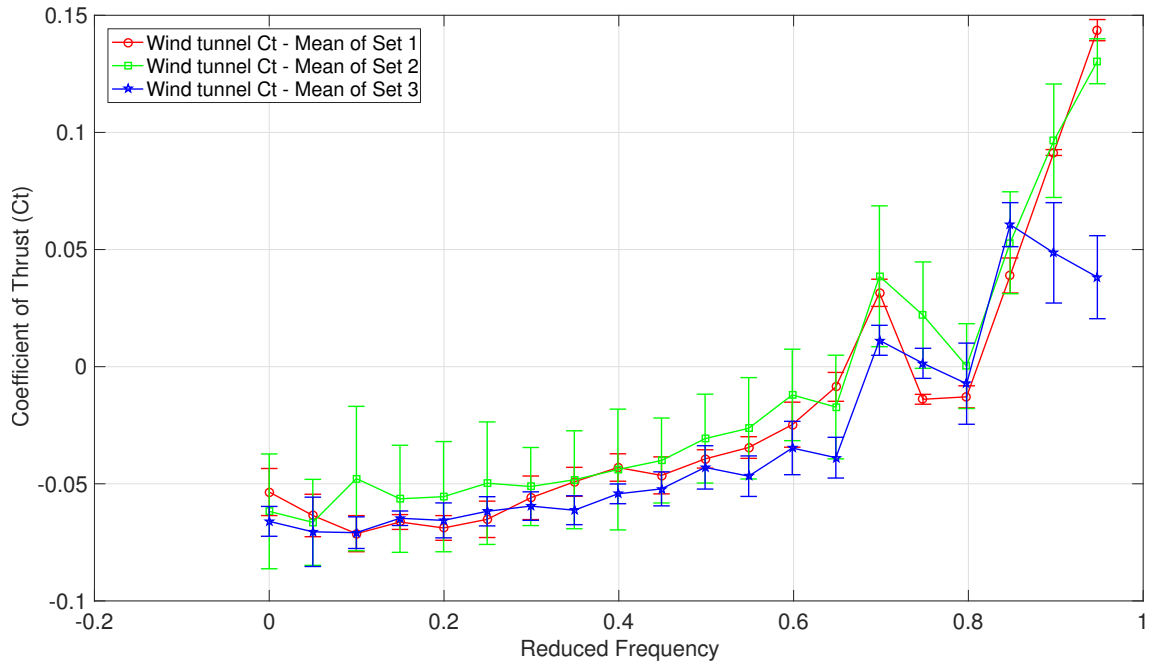


Figure 4.9: Coefficient of Thrust (with Standard Errors) vs Reduced Frequency for 50% Rigid Blue Wing.

The force measurement was observed to be a lot more scattered from set to set and trial to trial. In each of the graphs above, three sets of force data are shown, each of which are a mean of three trials of frequency sweep. As it can be seen, for each set of data, the error bounds are fairly large, and sometimes don't even overlap with another set. The error bounds of the mean C_T are large because the data scatter from trial to trial within each set is also large. Therefore, overall force data seems to be fairly repeatable but somewhat unreliable. Some of the expected sources of errors is the back and forth relocation of the actuation setup between wind tunnel and vacuum chamber causing load displacement issues on the force sensor. Another potential source of error could be an inherent bias of the force gage. As the wing is oscillated from low to high frequency, the force sensor is loaded increasingly until the testing is completed at a high flapping frequency. Even though, in the beginning of each trial of frequency sweep, the sensors are tared, the loading of the force sensor might cause it to follow a slightly different calibration slope each time leading to

potential error in the readings. The force sensor was also found to be very sensitive and could pick up very small disturbances from quite far away. Since the experiments were conducted in the open room where people could walk in and out, as well as other lab technicians could work on their own project, even the smallest vibration causing incident could be registered on the force gage during the experiments. All of these factors could potentially impact the quality of force sensor readings.

4.2.1 Digital Filtering of Force Sensor Data

Upon closer inspection of torque sensor and force sensor data using Fast Fourier Transform (FFT), it was noticed that the torque sensor data was not being influenced by any external high frequency noise, as it can be seen in Figure 4.12. However, the ATI force sensor reading was being influenced by some external high frequency noise at about $24Hz$. This can be observed in Figure 4.10, denoted by the large spike in the data at about $24Hz$. Ideally, a large spike in the FFT graph is only expected at the natural flapping frequency and its resonance frequencies. However, the spike observed at $24Hz$ meant that the force sensor readings would need to be filtered digitally. Therefore, a Butterworth filter was needed to be applied to the force sensor readings. An order of $N = 5$ and a cut-off frequency of $15Hz$ was chosen so as to not impact the low frequency contributions to the force sensor readings. The FFT of the force sensor reading after the application of Butterworth filter at $24Hz$ is shown in Figure 4.11.

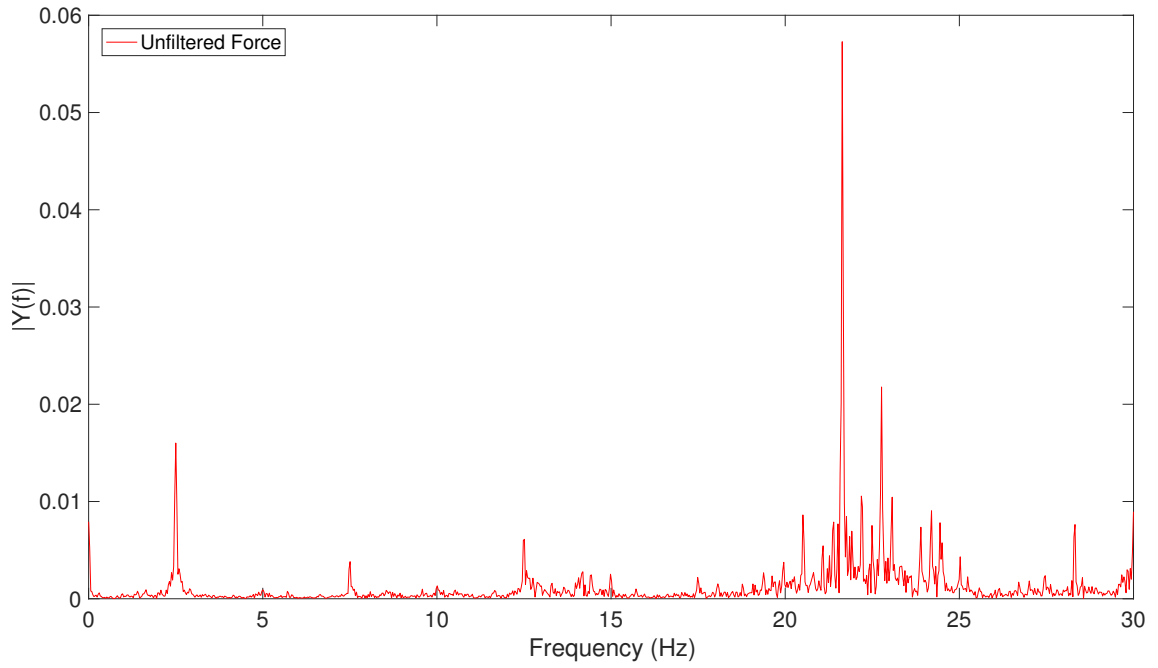


Figure 4.10: FFT of Unfiltered Force Reading at 2.5Hz Flapping Frequency.

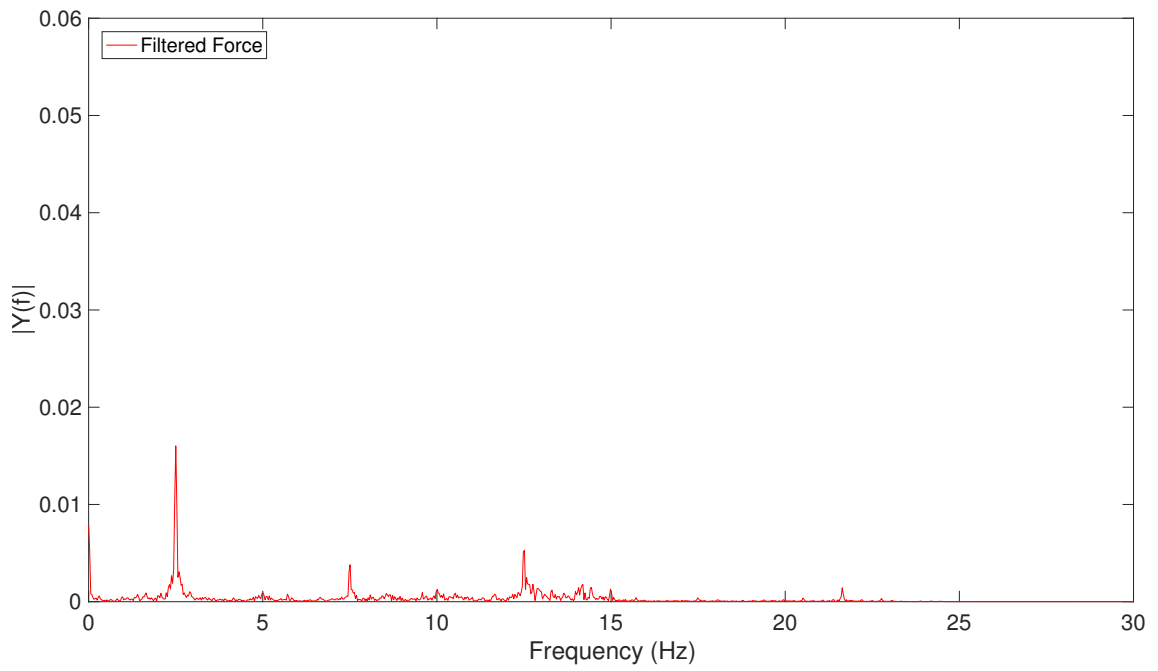


Figure 4.11: FFT of Filtered Force Reading at 2.5Hz Flapping Frequency.

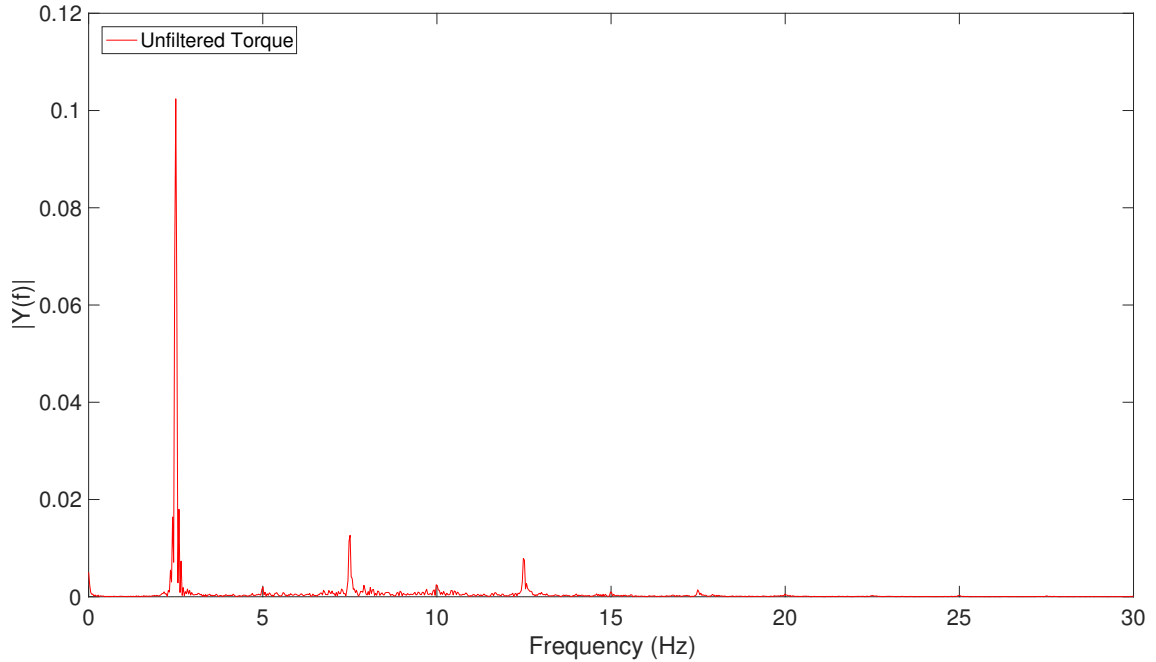


Figure 4.12: FFT of Unfiltered Torque Reading at 2.5Hz Flapping Frequency.

4.3 Number of Flapping Cycles Required for C_T Convergence

Initially, the software control as well as all the tests were designed to be run at five (5) ramp-up and ramp-down flapping cycles, along with twenty (20) steady state flapping cycles of desired amplitude and flapping frequency. However, upon studying the unrepeatability of the force sensor data, it was determined that the number of flapping cycles should be increased so as to improve the phase-average and time-average results of the force sensor readings.

To determine the number of cycles needed to achieve repeatable force readings, three trials of frequency sweep was run, each for different number of cycles, 15, 30, 60, 90, and 120. The coefficient of thrust values plotted against reduced frequency for various number of cycles is shown in Figure 4.13. As it can be observed, despite the outlier case of trial 3 for 120 cycles, the coefficient of thrust values seem to converge

with increasing number of cycles, especially above 60 cycles. Therefore, an optimal number of 100 flapping cycles was chosen for all future experiments.

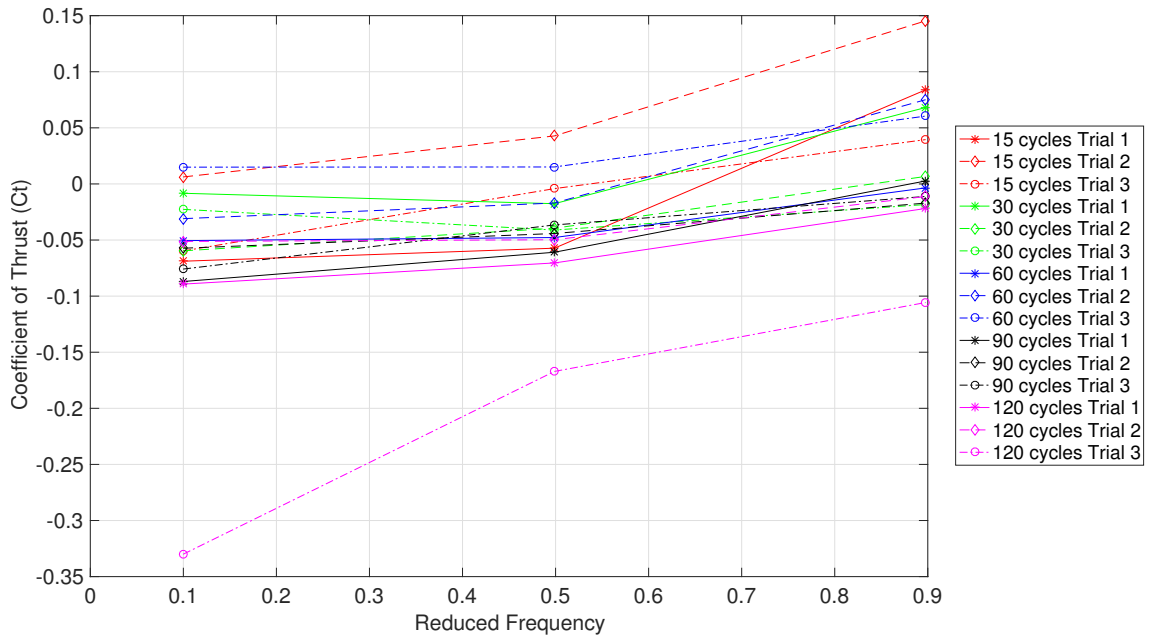


Figure 4.13: Test for Number of Flapping Cycles Required for C_T Convergence.

Chapter 5

Conclusions

The primary goal of developing an experimental system that could be used to generate flapping wing motion as well as perform measurements of unsteady forces and power was achieved successfully. This wind tunnel experimental setup can be used in performing a variety of flapping wing experiments. In addition, the secondary goal of developing a vacuum chamber system to measure inertial power of actuation system was also successfully achieved. The actuation system currently has the ability to perform flapping wing flight tests for a range of experimental regimes. Furthermore, the design of the wing has also been a successful feat. The current flat plate wing is a simple yet effective design that is easy and economical to fabricate.

From the results of the preliminary tests discussed in chapter 4, it can be observed that the force sensor data have large error bars and in some cases are also not very repeatable from one data set to another. This unrepeatability could be because of various sources of errors such as transfer of actuation setup between vacuum chamber and wind tunnel, external vibrations caused by humans walking by experimental setup, air compressor vibration and other factors that cause the sensitive ATI sensor to pick up external frequencies. Even though the external high frequency noise at about $24Hz$ was filtered out digitally, it was found that the results from the force sen-

sensor readings didn't alter significantly to improve repeatability. Therefore, while the Butterworth filter with 15Hz cutoff frequency is to be applied to all force sensor readings for future experiments, the sources of uncertainty for force sensor readings need to be examined thoroughly through more future experiments. In addition, the current experimental procedure of transferring experimental setup between wind tunnel and vacuum chamber needs to be streamlined. The force sensor reading is expected to be more repeatable trial to trial upon streamlining the experimental procedure.

In terms of torque sensors readings, it is clear that the power measurements using the torque sensor are very repeatable. In fact, the experimental procedure used in obtaining the preliminary data can be streamlined to minimize time spent on running experiments and maximize the numbers of wings tested. As discussed in section 3.2, currently, three sets of tests are run in both vacuum chamber and wind tunnel. Each set of test contains three trials of frequency sweep from low to high frequency. In between each set of trials, the actuation setup is transferred between the wind tunnel and vacuum chamber. This method was used to introduce maximum sources of errors and therefore, check the robustness of the system. As it can be seen from the scatter plots of Figure 4.1, 4.2 and 4.3, the torque sensor measurements are very repeatable from trial to trial. Therefore, moving forward, instead of running three sets of tests as well as transferring the actuation setup to/from wind tunnel and vacuum chamber in between every set, only one set of tests of five trials can be performed for both wind tunnel and vacuum chamber each. Similarly, in the preliminary tests, during each frequency test, the wing is flapped for 20 steady state cycles. Based on the results of the preliminary test in Figure 4.13, it is determined that all future experiments shall have 100 complete flapping cycles.

The overall system design is complete and robust. Flapping wing experiments can now be completed in both wind tunnel and vacuum chamber. It is however important to note that this system has its design limitations. Therefore, more tests need to be

performed to characterize the test system. As the wing flexion ratio changes, thus changing the wing mass, the amplitude output of the servo may vary. Because of this, the correction factor for the servo amplitude input may need to be tweaked. Similarly, more wings need to be tested to get a complete picture of role of wing flexibility on its performance.

5.1 Future Work

While the goal of designing and building a system capable of generating flapping wing motion and measuring unsteady force and power has been successfully achieved, the goal of understanding the physics of flexible wing flight remains unexplored. With the system design and development successfully completed, wings of varying flexion ratio and flexural rigidity now need to be tested at various wind conditions to understand the flow physics at a range of Reynold's Number. The current wing design of chordwise flexibility can be extended to incorporate spanwise flexibility as well as a mix of chordwise and spanwise flexibility to fully understand the role of wing flexibility in its performance. In addition, the aspect ratio of the wings can also be varied to get a better understanding of the role of wing flexibility and planform on its performance.

Bibliography

- S. Alben. Optimal flexibility of a flapping appendage in an inviscid fluid. *Journal of Fluid Mechanics*, 614:355–380, 2008.
- M. Bozkurttas, H. Dong, R. Mittal, P. Madden, and G. Lauder. Hydrodynamic performance of deformable fish fins and flapping foils. *AIAA*, 1392:1–11, 2006.
- S. P. Colin, J. H. Costello, J. O. Dabiri, A. Villanueva, J. B. Blottman, B. J. Gemmell, and S. Priya. Biomimetic and live medusae reveal the mechanistic advantages of a flexible bell margin. *PloS one*, 7(11):e48909, 2012.
- S. Combes and T. Daniel. Shape, flapping and flexion: wing and fin design for forward flight. *Journal of Experimental Biology*, 204(12):2073–2085, 2001.
- S. Combes and T. Daniel. Flexural stiffness in insect wings ii. spatial distribution and dynamic wing bending. *Journal of Experimental Biology*, 206(17):2989–2997, 2003.
- P. Corporation. Pololu maestro servo controller user’s guide, 2014. URL <https://www.pololu.com/docs/pdf/0J40/maestro.pdf>.
- H. Dai, H. Luo, P. J. F. de Sousa, and J. F. Doyle. Thrust performance of a flexible low-aspect-ratio pitching plate. *Physics of Fluids (1994-present)*, 24(10):101903, 2012.

- P. A. Dewey, B. M. Boschitsch, K. W. Moored, H. A. Stone, and A. J. Smits. Scaling laws for the thrust production of flexible pitching panels. *Journal of Fluid Mechanics*, 732:29–46, 2013.
- Ø. Endresen, E. Sjørgård, J. K. Sundet, S. B. Dalsøren, I. S. Isaksen, T. F. Berglen, and G. Gravir. Emission from international sea transportation and environmental impact. *Journal of Geophysical Research: Atmospheres*, 108(D17), 2003.
- F. E. Fish, G. V. Lauder, R. Mittal, A. H. Techet, M. S. Triantafyllou, J. A. Walker, and P. W. Webb. Conceptual design for the construction of a biorobotic auv based on biological hydrodynamics. In *13th International Symposium on Unmanned Untethered Submersible Technology, Durham, NH, Aug*, pages 24–27, 2003.
- S. Heathcote, Z. Wang, and I. Gursul. Effect of spanwise flexibility on flapping wing propulsion. *Journal of Fluids and Structures*, 24(2):183–199, 2008.
- D. H. Johnson. Wing loading in 15 species of north american owls. 1997.
- C.-K. Kang, H. Aono, C. E. Cesnik, and W. Shyy. Effects of flexibility on the aerodynamic performance of flapping wings. *Journal of fluid mechanics*, 689:32–74, 2011.
- T. Q. Le, J. H. Ko, D. Byun, S. H. Park, and H. C. Park. Effect of chord flexure on aerodynamic performance of a flapping wing. *Journal of Bionic Engineering*, 7(1): 87–94, 2010.
- M. Listak, G. Martin, D. Pugal, A. Aabloo, and M. Kruusmaa. Design of a semiautonomous biomimetic underwater vehicle for environmental monitoring. In *CIRA*, pages 9–14, 2005.
- P. Liu and N. Bose. Propulsive performance from oscillating propulsors with spanwise

- flexibility. In *Proceedings of the Royal Society of London A: Mathematical, Physical and Engineering Sciences*, volume 453, pages 1763–1770. The Royal Society, 1997.
- K. N. Lucas, N. Johnson, W. T. Beaulieu, E. Cathcart, G. Tirrell, S. P. Colin, B. J. Gemmell, J. O. Dabiri, and J. H. Costello. Bending rules for animal propulsion. *Nature communications*, 5, 2014.
- J.-M. Miao and M.-H. Ho. Effect of flexure on aerodynamic propulsive efficiency of flapping flexible airfoil. *Journal of Fluids and Structures*, 22(3):401–419, 2006.
- S. Michelin and S. G. L. Smith. Resonance and propulsion performance of a heaving flexible wing. *Physics of Fluids (1994-present)*, 21(7):071902, 2009.
- R. Mittal, H. Dong, M. Bozkurttas, G. Lauder, and P. Madden. Locomotion with flexible propulsors: Ii. computational modeling of pectoral fin swimming in sunfish. *Bioinspiration & biomimetics*, 1(4):S35, 2006.
- M. Nikolaev, A. Savitskiy, and Y. Senkin. Basics of calculation of the efficiency of a ship was propulsor of the wing type. *Sudostroenie*, 4:7–10, 1995.
- S. Ramananarivo, R. Godoy-Diana, and B. Thiria. Rather than resonance, flapping wing flyers may play on aerodynamics to improve performance. *Proceedings of the National Academy of Sciences*, 108(15):5964–5969, 2011.
- E. Sarradj, C. Fritzsche, and T. Geyer. Silent owl flight: bird flyover noise measurements. *AIAA journal*, 49(4):769–779, 2011.
- J. L. Tangorra, G. V. Lauder, I. W. Hunter, R. Mittal, P. G. Madden, and M. Bozkurttas. The effect of fin ray flexural rigidity on the propulsive forces generated by a biorobotic fish pectoral fin. *Journal of Experimental Biology*, 213(23):4043–4054, 2010.

- J. Toomey and J. D. Eldredge. Numerical and experimental study of the fluid dynamics of a flapping wing with low order flexibility. *Physics of Fluids (1994-present)*, 20(7):073603, 2008.
- M. Vanella, T. Fitzgerald, S. Preidikman, E. Balaras, and B. Balachandran. Influence of flexibility on the aerodynamic performance of a hovering wing. *Journal of Experimental Biology*, 212(1):95–105, 2009.
- A. Villanueva, C. Smith, and S. Priya. A biomimetic robotic jellyfish (robojelly) actuated by shape memory alloy composite actuators. *Bioinspiration & biomimetics*, 6(3):036004, 2011.
- J. Young, S. M. Walker, R. J. Bomphrey, G. K. Taylor, and A. L. Thomas. Details of insect wing design and deformation enhance aerodynamic function and flight efficiency. *Science*, 325(5947):1549–1552, 2009.

Appendix A

Amplitude Calibration

Due to the undershooting and overshooting nature of the servo at various experimental conditions, it is important to amplify or deamplify the prescribed amplitude to reach the desired amplitude. This gives rise to two amplitudes in experimental context: Desired Amplitude and Corrected Amplitude. First, the servo is commanded to generate the desired motion at some target frequency and desired amplitude. Using the optical encoder data, the output amplitude of the harmonic motion is determined which, due to its physical limitations, is different than the desired amplitude. The scaling factor between the desired amplitude and servo output amplitude can then be obtained. Using this scaling factor, a new corrected amplitude is calculated and prescribed to the servo at the same frequency. This makes the servo undershoot when it would have originally overshoot, or vice versa, thereby achieving the correct desired amplitude.

Although this is a two step process, meaning, same motion has to be carried out twice for any given frequency, amplitude, and wing loading condition during the testing, this method has proven to be very robust. In fact, using the amplitude correction method, the percentage difference between the desired amplitude and the output amplitude after correction is usually under 1%, but always within 3%, as it

can be observed in Figure A.1. However, it is important to note that when the wing masses change significantly, this procedure may need to be tweaked as well to account for heavier or lighter wings. The basic formula used for finding the corrected angle is:

$$correctedAmp = ((1 - realAmp/idealAmp) * idealAmp) + idealAmp; \quad (A.1)$$

where *idealAmp* is the ideal peak to peak flapping amplitude desired for the experiment, *realAmp* is the output amplitude of the servo calculated from the optical encoder data of the first test run, and *correctedAmp* is the corrected (amplified/deamplified) amplitude that is to be input on the second run for the servo to actually achieve the ideal amplitude.

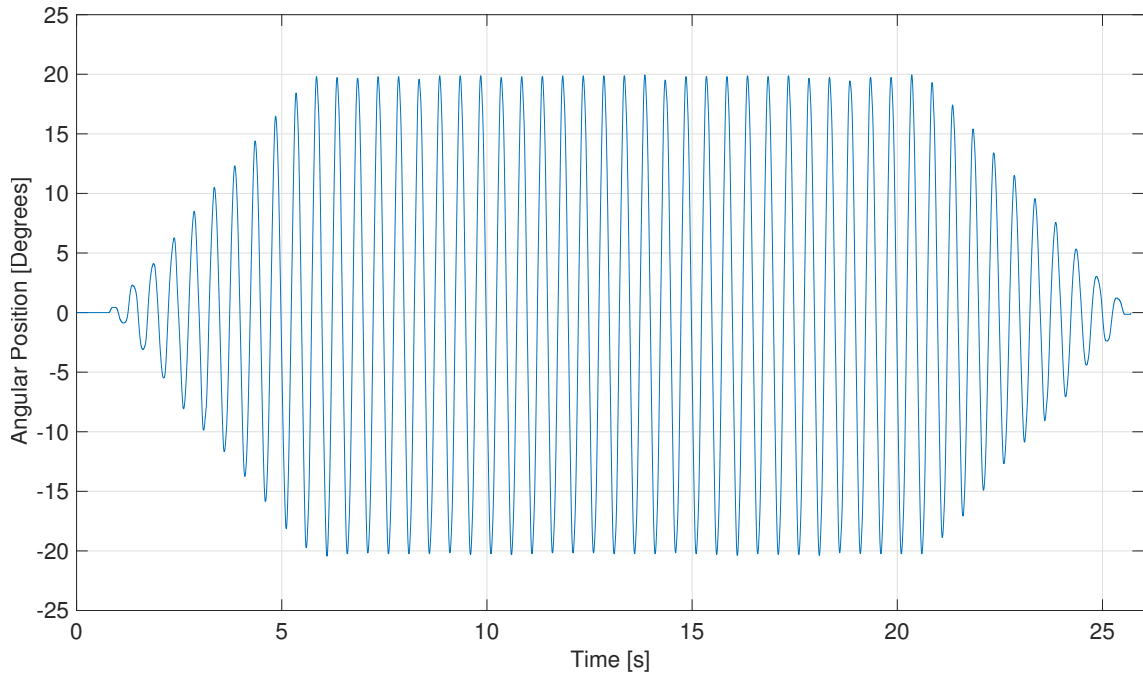


Figure A.1: Post Amplitude Calibration Servo Position Output vs Time

Vita

DURLAV MUDBHARI

Date of Birth: March 15, 1992

Email: DurlavMudbhari@gmail.com

Place of Birth: Nuwakot, Nepal

Website: www.DurlavMudbhari.com

Parents: Mira Mudbhari and Bishwa Raj Mudbhari

EDUCATION

Master of Science, *Highest Honors*

Mechanical Engineering, Lehigh University, January 2017

Bachelor of Science, *Highest Honors*

Integrated Business and Engineering (Economics), Lehigh University, August 2015

Bachelor of Science, *Highest Honors*

Mechanical Engineering (Aerospace concentration), Lehigh University, May 2015

EXPERIENCE

Mechanical Design Engineer II, Gulfstream Aerospace, Oct 2016 - Present

Mechanical Design Engineer Intern, Gulfstream Aerospace, June - Aug 2014

Undergraduate Research Assistant, BDSI, Lehigh University, June - Aug 2013

Mechanical Design Engineer Intern, Dent Design Hardware, May - Aug 2012

Co-President, Lehigh Aerospace Club, Fall 2013 - Spring 2015